

# Perihelion Activity of (3200) Phaethon Is Not Dusty: Evidence from STEREO/COR2 Observations

MAN-TO HUI (許文韜)<sup>1</sup>

<sup>1</sup>*State Key Laboratory of Lunar and Planetary Science, Macau University of Science and Technology, Avenida Wai Long, Taipa, Macau*

(Received 2022; Revised November 23, 2022; Accepted 2022)

## ABSTRACT

We present an analysis of asteroid (3200) Phaethon using coronagraphic observations from 2008 to 2022 by the COR2 cameras onboard the twin Solar TERrestrial RELations Observatory (STEREO) spacecraft. Although the asteroid cannot be confidently detected in individual images, we managed to spot it in stacks combined from the same sets of perihelion observations, yet only at small ( $\lesssim 30^\circ$ ) but not large ( $\gtrsim 150^\circ$ ) phase angles. The lack of forward scattering that should have occurred to dust grains having sizes comparable to transmitted wavelengths causes serious incompatibilities between the amounts and properties of dust inferred from the HI-1 and COR2 observations, implying that the perihelion activity of Phaethon is highly likely irrelevant to the ejection of dust grains suggested by earlier studies based on STEREO's HI-1 observations alone. Rather, we deduce that the observed perihelion activity is from some gas emissions, possibly Fe I and/or Na D lines, the latter of which may have become transmittable due to an ageing effect of the HI-1 filters. The modelled emission flux is qualitatively similar to the HI-1 observations in the case where the peak of the atomic production rate is delayed by  $\sim 1$  day from perihelion. In order to verify our conjecture, as well as to fully understand the perihelion activity of Phaethon, more observations at small heliocentric distances will be needed. To facilitate future ground observations, we compile a list of observing windows ideal for the search of gas emissions of the asteroid. The best opportunities will be during total solar eclipses.

*Keywords:* asteroids: individual (Phaethon) — methods: data analysis

## 1. INTRODUCTION

(3200) Phaethon is a near-Earth asteroid discovered by the Infrared Astronomical Satellite in 1983 (Green & Kowal 1983). Its current orbit is highly elongated with an orbital eccentricity of  $e = 0.89$  and a semimajor axis of  $a = 1.27$  au, resulting in a perihelion distance of merely  $q = 0.14$  au. Phaethon is identified to be dynamically associated with the Geminid meteoroid stream (Whipple 1983; Williams & Wu 1993), in contrast to most of other meteoroid streams, whose parent bodies are comets (Jenniskens 2006). Ohtsuka et al. (2006, 2008) suggested that two additional asteroids 2005 UD and 1999 YC are potentially split fragments of Phaethon, together with Phaethon and the Geminids constituting the Phaethon-Geminid Complex (PGC). Various deep imaging searches for dust ejecta and gas emissions of Phaethon were carried out, returning only negative results (Chamberlin et al. 1996; Cochran & Barker 1984; Hsieh & Jewitt 2005; Jewitt et al. 2018, 2019; Tabeshian et al. 2019; Wiegert et al. 2008; Ye et al. 2018, 2021). However, Jewitt & Li (2010), Jewitt et al. (2013), Li & Jewitt (2013), and Hui & Li (2017) reported that Phaethon underwent anomalous brightening and exhibited a tiny tail in the antisolar direction around its perihelion passages in 2009, 2012, and 2016 in observations taken by spacecraft Solar TERrestrial RELations Observatory (STEREO), possibly due to the ejection of  $\sim 1 \mu\text{m}$  sized dust caused by thermal fracture. They all agreed that the observed perihelion activity is likely irrelevant to the Geminid meteoroid stream, because the estimated dust size is too small compared to the Geminids and the estimated mass loss is also too small to sustain the stream effectively. Nonetheless, Phaethon is

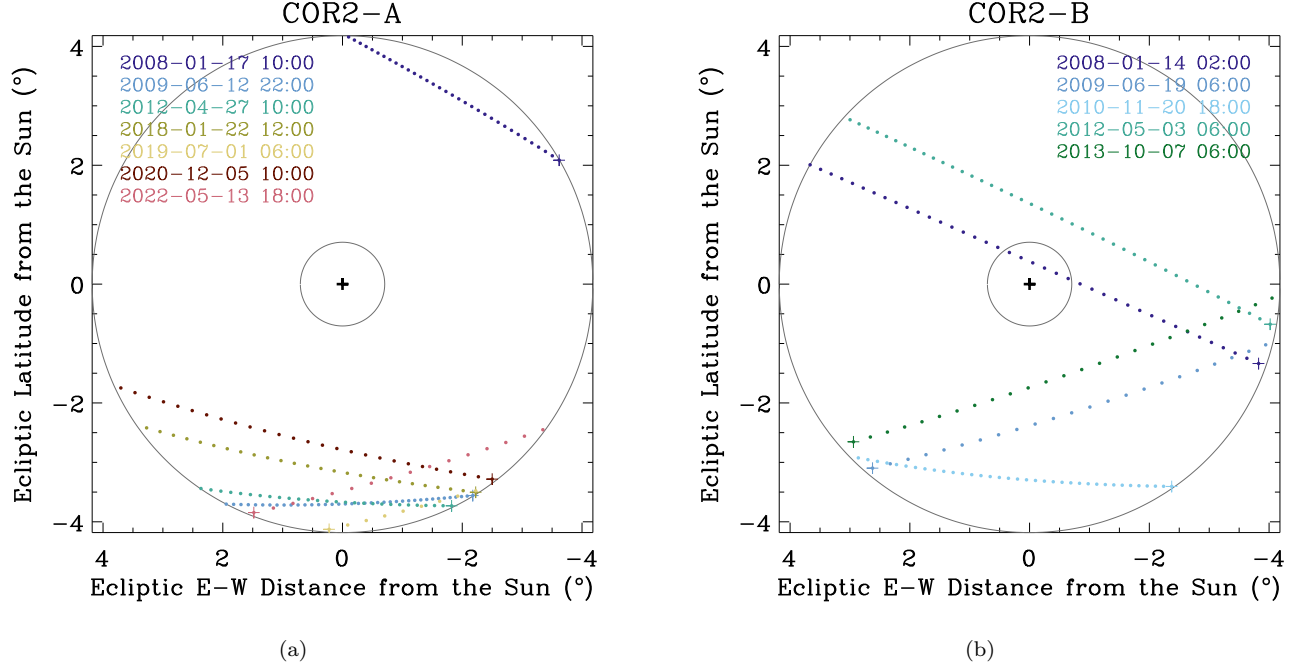


**Figure 1.** Transits of Phaethon in the annular FOVs (bounded by two concentric circles) of (a) COR2-A and (b) and COR2-B cameras. Trajectories from different apparitions are distinguished by different colours. The positions are plotted every two hours, with the first positions inside the FOVs indicated by symbol “+” in the same colours. Corresponding epochs in UTC are given in the legends. The bold plus sign in black at the centre of either panel represents the centre of the Sun.

indisputably classified as an active asteroid (Jewitt 2012). Besides, the dust trail along its orbit was recently observed at infrared and optical wavelengths (Arendt 2014; Battams et al. 2020, 2022). Despite being consistent with the Geminid meteoroid stream, the dust trail slightly deviates from the orbit of Phaethon (Battams et al. 2022).

While the quest for the processes by which Phaethon produced the Geminid meteoroid stream (and other PGC members also) is by no means near the end, in this paper, we turn our primary focus on the near-Sun activity of Phaethon. The question whether the activity observed in HI-1 observations is attributed to the dust ejection remained unsettled, as the tail of Phaethon reminded us of the one of Mercury. While the tail of Phaethon was convincingly visible around perihelion in images taken by the camera Heliospheric Imager-1 (HI-1; Eyles et al. 2009) onboard STEREO, occasionally Mercury was seen to exhibit a similar albeit much brighter anti-sunward tail for reasons not yet fully understood (Schmidt 2013). One hypothesis Schmidt (2013) put forward is that the filter bandpasses of the HI-1 cameras have changed since launch, allowing for nontrivial transmission of sodium D-lines. Here, we investigate coronagraphic observations of Phaethon from STEREO, including those taken at never-before-seen large phase angles for the object, to revisit its perihelion activity and identify the dominant driving source thereof. Our paper is organised in the following manner. We will detail the coronagraphic observations and data reduction in Section 2, followed by an analysis of the observations in Section 3. Discussion is held in Section 4 and the summary is presented in Section 5.

## 2. OBSERVATIONS & DATA REDUCTION

STEREO (Kaiser et al. 2008) consists of twin solar probes moving in Earth-like heliocentric orbits yet in opposite directions with respect to Earth. The one leading Earth is STEREO-A, and the other one is STEREO-B. Both of the spacecraft carry the Sun Earth Connection Coronal and Heliospheric Investigation (SECCHI) onboard, which is a suite of five different telescopes, including an extreme ultraviolet imager EUVI, two Lyot coronagraphs COR1 and COR2, and two heliospheric imagers HI-1 and HI-2 (Howard et al. 2008). Since 2014 October, communication with

**Table 1.** Observing Geometry of Phaethon

Apparition	Date & Time <sup>a</sup> (UT)	Camera	Heliocentric Distance <sup>b</sup> $r_H$ (au)	Observer-centric Distance <sup>c</sup> $\Delta$ (au)	Phase Angle <sup>d</sup> $\alpha$ (°)	Visibility
2008	Jan 17 10:38 – Jan 20 03:38	COR2-A	0.206 → 0.286	[1.159, 1.242]	[14.0, 19.9]	✓
	Jan 14 01:08 – Jan 17 08:08	COR2-B	0.140 → 0.203	[1.124, 1.192]	[4.4, 31.2]	✓
2009	Jun 12 22:38 – Jun 16 00:08	COR2-A	0.315 → 0.225	[1.168, 1.262]	[12.6, 17.8]	✓
	Jun 19 04:53 – Jun 21 02:38	COR2-B	0.148 $\xrightarrow{p}$ 0.144	[0.912, 0.922]	[148.3, 162.7]	X
2010	Nov 20 18:24 – Nov 23 18:24	COR2-B	0.245 → 0.163	[1.219, 1.309]	[17.3, 28.9]	✓
2012	Apr 27 10:24 – Apr 29 14:54	COR2-A	0.242 → 0.180	[1.121, 1.186]	[16.3, 22.5]	✓
	May 3 05:24 – May 6 19:54	COR2-B	0.145 → 0.231	[1.125, 1.217]	[6.9, 29.9]	✓
2013	Oct 7 04:24 – Oct 9 06:24	COR2-B	0.143 $\xrightarrow{p}$ 0.152	[0.919, 0.933]	[147.5, 167.6]	X
2018	Jan 22 12:24 – Jan 24 14:54	COR2-A	0.184 → 0.143	[1.082, 1.126]	[18.9, 28.8]	✓
2019	Jul 1 05:39 – Jul 1 21:54	COR2-A	0.159 → 0.148	[0.819, 0.832]	[152.0, 154.4]	X
2020	Dec 5 10:24 – Dec 7 14:39	COR2-A	0.168 $\xrightarrow{p}$ 0.140	[1.079, 1.111]	[17.8, 29.7]	✓
2022	May 13 17:39 – May 14 20:54	COR2-A	0.153 → 0.141	[0.824, 0.836]	[152.4, 157.1]	X

<sup>a</sup>Timestamps of the first and last available images in which Phaethon was apparently inside the outer edge of the camera’s FOV.

<sup>b</sup>The first and last numbers respectively correspond to the heliocentric distances of Phaethon in the first and last available images. If the perihelion passage was covered in the FOV, a letter “p” is inserted in between above the arrow.

<sup>c</sup>The interval gives the observed minimum and maximum observer-centric distances, not necessarily corresponding to the distances of Phaethon in the first and last available images from the apparition.

<sup>d</sup>The angle of Sun-Phaethon-observer. The interval simply shows the observed minimum and maximum phase angles.

STEREO-B has been lost due to hardware anomalies.<sup>1</sup> In our paper, only COR2 and HI-1 are the relevant telescopes, and the others will be ignored.

Phaethon has been studied using observations taken by both HI-1 cameras (Jewitt & Li 2010; Li & Jewitt 2013; Jewitt et al. 2013; Hui & Li 2017). These images have an angular resolution of  $\sim 70''$  pixel<sup>-1</sup> and covered a square field of view (FOV) of  $\sim 20^\circ \times 20^\circ$  along the ecliptic at solar elongations between  $\sim 4^\circ$  and  $24^\circ$  (Eyles et al. 2009). On the contrary, observations of Phaethon in the COR2 cameras onboard STEREO-A and STEREO-B (labeled COR2-A and COR2-B, respectively) have never been previously reported. Both cameras monitor an annular region of  $\sim 2.5$ – $15 R_\odot$  (where  $R_\odot$  is the apparent solar radius at a heliocentric distance of 1 au, or  $\sim 0.7$ – $4.0$ ) with the Sun blocked at the centre. The effective bandpasses of the cameras are both  $\sim 650$ – $750$  nm (Howard et al. 2008).

Using JPL Horizons’ solution to the orbit of Phaethon, we identified that the object has also transited the FOVs of COR2-A and COR2-B around perihelion multiple times since the spacecraft became operational, including four apparitions at large phase angles ( $\alpha \gtrsim 150^\circ$ ), placing interplanetary dust in a regime where strong forward-scattering enhancements would occur (Kolokolova et al. 2004; Marcus 2007). We show the apparent trajectories of Phaethon within the FOVs of COR2-A and COR2-B in Figure 1 and tabulate the observing geometry in Table 1. Accordingly, we collected the COR2 total brightness images around the time of the transits of Phaethon. All of these level-0.5 Flexible Image Transport System (FITS) images are  $2048 \times 2048$  pixels in size in an unbinned mode and have a pixel scale of  $14''$  and an individual exposure of 6 seconds in duration.

The images were first calibrated by bias subtraction and vignetting correction and then normalised by the exposure time in IDL using SolarSoftWare (SSW; Freeland & Handy 1998). Next, in order to maximally suppress the corona, we computed a median background for each calibrated image from neighbouring individual exposures, which was subsequently subtracted from the calibrated image. The resulting images are basically free from artifacts, in which background stars are clearly visible. Only slight residuals of time-varying fine features of the corona remained near the

<sup>1</sup> [https://stereo-ssc.nascom.nasa.gov/behind\\_status.shtml](https://stereo-ssc.nascom.nasa.gov/behind_status.shtml)

inner edge of the annular FOV in some of the images, but they posed no strong influence on our study of Phaethon on most occasions. Despite that the astrometric information is available in the FITS file headers, we noticed that the accuracy tended to decline towards the edge of the images due to the field distortion, as catalogued and observed field stars thereabouts showed visible positional discrepancies of a few pixels at worst. Thus, astrometric calibration of the images was performed with the software package `astrometry.net` (Lang et al. 2010), resulting in improved solutions via visual inspection.

We attempted to search for Phaethon by visually examining individual COR2 images in which Phaethon was in the FOV, but we were unable to robustly detect it above the noise level around the ephemeris positions. In order to maximally suppress noise, we combined all of these images taken by the same cameras in the same apparitions with respect to the calculated apparent motion of Phaethon. We thereby managed to immediately identify the target at the exact calculated ephemeris positions in the stacks obtained at small phase angles, as it was basically the brightest object therein. The FWHM of Phaethon was measured to be consistent with those of field stars in individual images,  $\sim 2\text{--}3$  pixels. In contrast, we were unable to spot Phaethon in the stacks combined from images taken at large phase angles. In Figure 2 we show the combined images of Phaethon, including the nondetections. The visibility is summarised both in Tables 1 and 2 for convenience.

One may notice an observational bias from Table 2 that the stacks which show Phaethon were combined from systematically more individual images than those that do not. To get rid of the bias, we evenly divided individual images taken by the same cameras from the same apparitions in which Phaethon was visible in the final stacks into two groups, if the total numbers of images covering Phaethon are less than 200, otherwise three groups. Then, we still combined individual images from each group into a new stack with alignment on the ephemeris motion of Phaethon. As a result, we were still able to see Phaethon at the predicted positions in all but three (one from 2008 by COR2-A, and the two others from 2012 by COR2-B) of the new stacks. The three stacks showing no hint of Phaethon were combined from individual exposures where Phaethon was  $\gtrsim 0.2$  au from the Sun, further than in any other images. Therefore, we can firmly rule out the possibility that the visibility of Phaethon is caused by the observational bias. Rather, it indicates the authentic apparent brightness of the asteroid.

### 3. ANALYSIS

#### 3.1. Photometry

In order to convert the observed flux (in  $\text{DN s}^{-1}$ ) to the apparent magnitude of Phaethon, accurate image zero-points of COR2-A and COR2-B would be needed. However, there were only preliminary results from pre-flight tests. Therefore, we had to determine the image zero-points by performing photometry of field stars in individual images. The apparent magnitude and the observed flux of a star (labeled by the symbol “\*”) in a COR2 image, denoted as  $m_*$  and  $F_*$ , respectively, are related to the image zero-point  $m_0$  by

$$m_* = \underbrace{-2.5 \log F_*}_{\tilde{m}_*} + m_0, \quad (1)$$

in which  $\tilde{m}_* = -2.5 \log F_*$  is the instrumental magnitude of the star. Since the measured pre-flight effective bandpasses of the COR2 cameras are different from any photometric standard, we adopted the colour mixing method in Bewsher et al. (2010) and approximated the apparent magnitude of some star in the COR2 bandpass as a linear combination of the apparent magnitudes of the star in three different photometric standard bandpasses, i.e.,

$$m_* = \sum_{j=1}^3 \mathcal{C}_j m_{*,j}, \quad (2)$$

where  $\mathcal{C}_j$  ( $j = 1, 2, 3$ ) is the linear coefficient in the  $j$ -th band. With multiple field stars, the linear coefficients and the image zero-point can be determined by minimising the goodness of fit

$$\chi^2 = \sum_k \frac{\left[ \tilde{m}_{*k} + m_0 - \sum_{j=1}^3 \mathcal{C}_j m_{*,j,k} \right]^2}{(\Delta \tilde{m}_{*k})^2 + \sum_{j=1}^3 (\mathcal{C}_j \Delta m_{*,j,k})^2}. \quad (3)$$

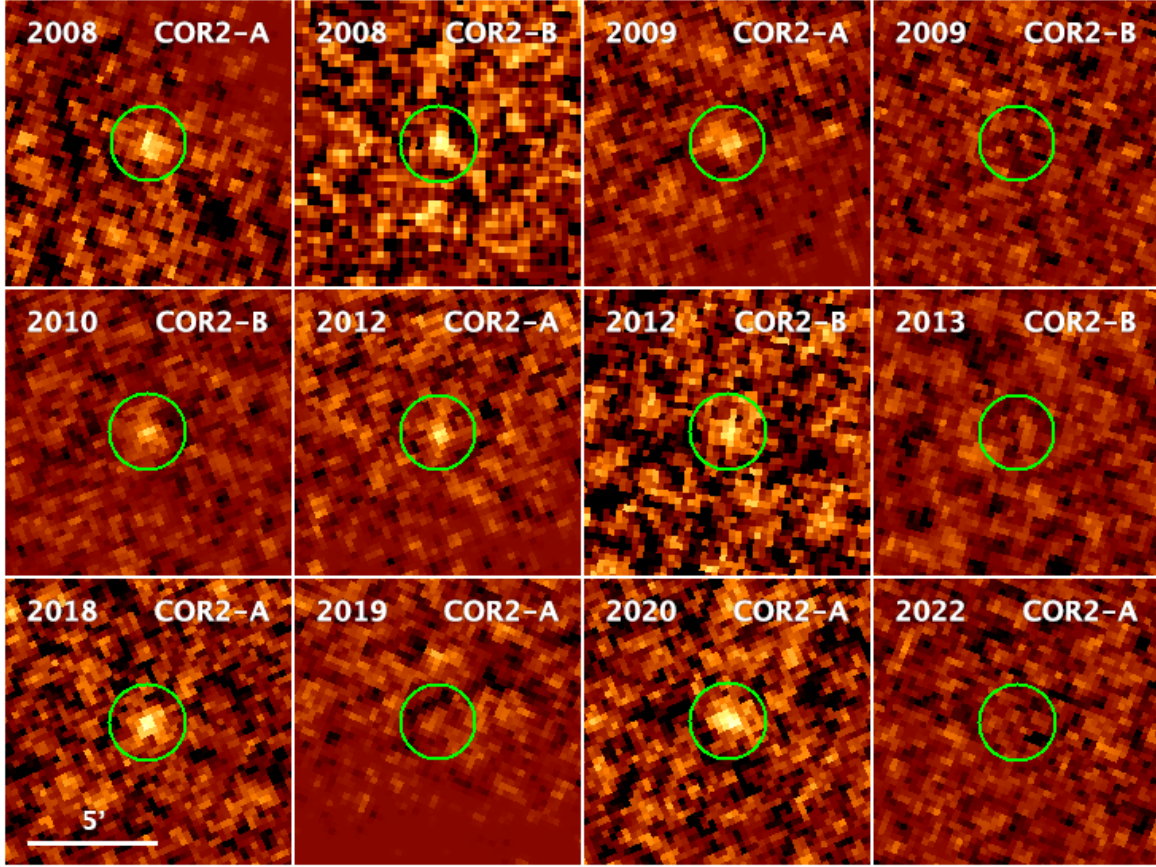


**Figure 2.** Phaethon in COR2 images around different perihelion returns. The images are median stacks from individual images taken by the same cameras in the same apparitions with alignment on the ephemeris motion of Phaethon (marked by a green circle in each panel). We are unable to confidently detect Phaethon in the observations taken at large phase angles (COR2-B in the apparitions of 2009 and 2013, COR2-A in 2019 and 2022). J2000 equatorial north is up and east is left. A scale bar of 5' in length applicable to all of the panels is shown in the lower left corner.

Here,  $\Delta\tilde{m}_{*k}$  and  $\Delta m_{*k,j}$  are the uncertainties in the instrumental magnitude and the apparent magnitude in the  $j$ -th band, respectively, of the  $k$ -th star ( $*_k$ ) in the image.

The observed fluxes of field stars were measured using a circular aperture of 3 pixels in radius, whose uncertainties were obtained by propagating errors from the Poisson statistics and fluctuation in the sky background measured from an annular region from  $1.5\times$  to  $2.5\times$  the aperture radius to the centre. Given the effective bandpasses of the COR2 cameras, we set  $\mathcal{C}_j$  ( $j = 1, 2, 3$ ) respectively correspond to the linear coefficients for  $g$ ,  $r$ , and  $i$ -band star magnitudes in the Pan-STARRS photometric system from the ATLAS All-Sky Stellar Reference Catalog (Refcat2; Tonry et al. 2018) for photometric calibration. The Levenberg-Marquardt optimisation routine MPFIT (Markwardt 2009) was exploited to obtain the best-fit photometric parameters along with their uncertainties for each of the COR2 images. During initial tests, we found that MPFIT would converge to different local minima with slightly different initial guesses for the parameters to be solved and yet their  $\chi^2$  values were comparable. Also given the fact that the COR2 bandpasses largely overlap with the  $r$  band in the Pan-STARRS photometric system, we thus fixed  $\mathcal{C}_2 \equiv 1$  and performed the optimisation for other parameters. Stars fainter than  $\sim 9.5$  mag in the three bands and those with magnitudes of observed-minus-calculated residuals over  $3\sigma$  were discarded.

Figure 3 shows a typical example of the best-fit results for a COR2 image and the columns under “Best-fit Photometric Parameters” in Table 2 are a summary of our best-fit results of the photometric calibration. We have verified that the best-fit results are robust, as adjusting settings such as the size of the photometric aperture and the cutoff threshold for outlier rejection would not alter the best-fit results over their respective uncertainties whatsoever. We plot the best-fit image zero-points in Figure 4 to investigate if there is an ageing effect that causes a drift therein over



**Table 2.** Summary of Photometric Calibration and Observations of Phaethon

Apparition	Camera	Number of Images <sup>a</sup>	Observations of Phaethon			Best-fit Photometric Parameters		
			Visibility	App. Mag. <sup>b</sup> $\bar{m}$	Cross-section <sup>c</sup> $\Xi_d$ (m <sup>2</sup> )	Zero-point $m_0$	Linear Coefficients	
2008	COR2-A	186 (131)	✓	$11.17 \pm 0.22$	$(6.3 \pm 7.9) \times 10^7$	$12.81 \pm 0.12$	$-0.261 \pm 0.019$	$+0.199 \pm 0.026$
	COR2-B	222 (120)	✓	$10.83 \pm 0.27$	$(2.0 \pm 3.5) \times 10^7$	$12.67 \pm 0.12$	$-0.277 \pm 0.013$	$+0.217 \pm 0.014$
2009	COR2-A	250 (148)	✓	$11.48 \pm 0.22$	$(5.4 \pm 6.9) \times 10^7$	$12.98 \pm 0.15$	$-0.249 \pm 0.031$	$+0.219 \pm 0.026$
	COR2-B	144 (94)	X	$\geq 12.30 \pm 0.18$	$\leq (9.6 \pm 10.4) \times 10^4$	$12.93 \pm 0.13$	$-0.236 \pm 0.021$	$+0.212 \pm 0.023$
2010	COR2-B	282 (217)	✓	$11.60 \pm 0.25$	$(2.5 \pm 3.8) \times 10^7$	$12.84 \pm 0.12$	$-0.256 \pm 0.023$	$+0.229 \pm 0.021$
2012	COR2-A	208 (157)	✓	$11.73 \pm 0.25$	$(2.2 \pm 3.4) \times 10^7$	$12.96 \pm 0.10$	$-0.256 \pm 0.021$	$+0.227 \pm 0.021$
	COR2-B	282 (261)	✓	$11.17 \pm 0.30$	$(1.9 \pm 3.3) \times 10^7$	$12.89 \pm 0.09$	$-0.280 \pm 0.017$	$+0.263 \pm 0.023$
2013	COR2-B	136 (95)	X	$\geq 12.37 \pm 0.18$	$\leq (5.3 \pm 5.8) \times 10^4$	$13.15 \pm 0.14$	$-0.279 \pm 0.024$	$+0.298 \pm 0.027$
2018	COR2-A	198 (141)	✓	$11.01 \pm 0.21$	$(2.7 \pm 3.9) \times 10^7$	$12.88 \pm 0.15$	$-0.259 \pm 0.033$	$+0.220 \pm 0.039$
2019	COR2-A	93 (50)	X	$\geq 12.49 \pm 0.15$	$\leq (1.6 \pm 1.7) \times 10^5$	$12.96 \pm 0.15$	$-0.241 \pm 0.032$	$+0.217 \pm 0.039$
2020	COR2-A	213 (160)	✓	$10.77 \pm 0.21$	$(3.0 \pm 4.2) \times 10^7$	$13.01 \pm 0.12$	$-0.228 \pm 0.026$	$+0.208 \pm 0.028$
2022	COR2-A	155 (84)	X	$\geq 12.49 \pm 0.15$	$\leq (1.2 \pm 1.3) \times 10^5$	$13.06 \pm 0.11$	$-0.254 \pm 0.029$	$+0.239 \pm 0.031$
Overall	COR2-A	1303	N/A			$12.96 \pm 0.15$	$-0.251 \pm 0.029$	$+0.219 \pm 0.031$
	COR2-B	1066	N/A			$12.88 \pm 0.18$	$-0.271 \pm 0.024$	$+0.246 \pm 0.036$

<sup>a</sup>Numbers of images used for photometric calibration (unbracketed) and combined for Phaethon (bracketed).

<sup>b</sup>Apparent magnitude of Phaethon in the COR2 bandpasses.

<sup>c</sup>Effective scattering cross-section of ejected dust.

NOTE— Parameters  $C_j$  ( $j = 1, 2, 3$ ) correspond to the linear coefficients for the  $g$ ,  $r$ , and  $i$ -band star magnitudes in the Pan-STARRS photometric system. We set  $C_2 \equiv 1$  in the Levenberg-Marquardt optimisation. The reported values of the image zero-points and linear coefficients and the associated errors are weighted means and standard deviations, respectively. Values in photometry of Phaethon preceded by inequality signs are  $3\sigma$  values.

the course of the past multiple perihelion returns of Phaethon. Although we can spot some temporal variations, they are not significantly greater than the uncertainties. We repeated the aforementioned procedures yet with slightly larger circular apertures for photometry, finding that the results remained unchanged within the respective uncertainty levels. Therefore, we conclude that the ageing effect of the COR2 cameras is negligible in comparison to the uncertainties in photometric measurements. We calculated the weighted mean and standard deviation values of the photometric parameters for all of the COR2-A and COR2-B images separately (Table 2), which we adopted to obtain the apparent magnitude of Phaethon (see the column “App. Mag.” in Table 2). In cases of the nondetections,  $3\sigma$  lower limits are given instead.

### 3.2. Activity

Following the argument that the perihelion activity of Phaethon is caused by dust ejection (Jewitt & Li 2010; Li & Jewitt 2013; Jewitt et al. 2013; Hui & Li 2017), we estimated the effective cross-section of ejected dust that would be needed to account for the observed brightness of the object in the COR2 cameras. Given the light scattering properties and size distribution of cometary dust (Fulle 2004; Kolokolova et al. 2004), any ejected dust having sizes comparable to the transmitted wavelengths (i.e.,  $\sim 1 \mu\text{m}$ ) should most likely dominate the brightness excess of Phaethon, if there were any. The bandpasses of the COR2 cameras also guarantee that the observed signal is basically from dust scattering of sunlight alone and minimise any possibility of contamination due to gaseous emission lines that are typically seen for comets.

At some instant, the effective cross-section of the ejected dust  $\Xi_d$  is related to the apparent magnitude of Phaethon  $m$  by

$$\Xi_d = \frac{\pi}{\phi_d(\alpha)} \left[ \frac{r_H^2 \Delta^2}{pr_\oplus^2} 10^{0.4(m_\odot - m)} - \phi_n(\alpha) R_n^2 \right]. \quad (4)$$

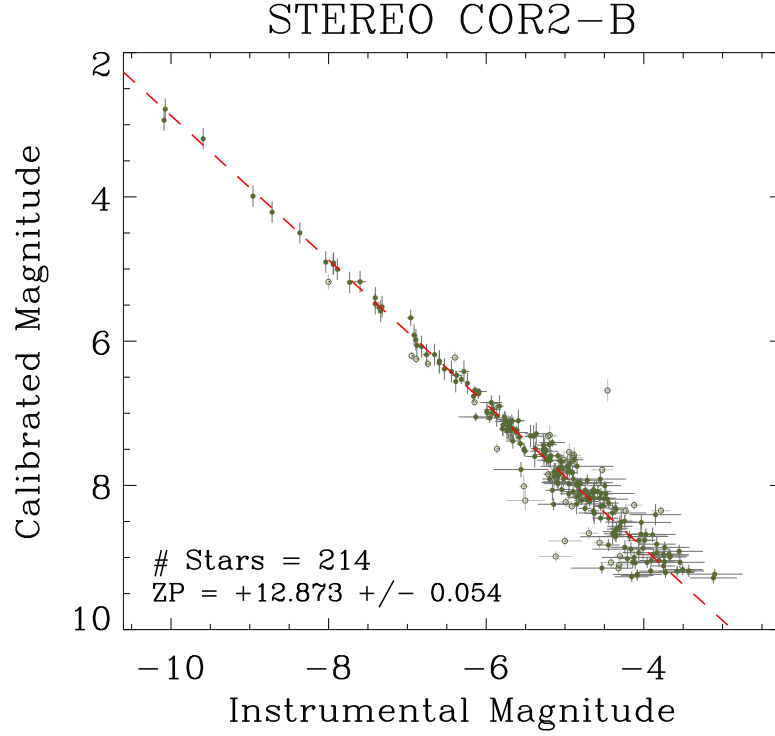


**Figure 3.** Example of fitting the photometric parameters for a COR2-B image from 2012 May 3. Field stars used and rejected in the Levenberg-Marquardt optimisation are plotted as olive closed and open circles, respectively. The best-fit function is shown as the red dashed line. In the lower left corner, we present the number of used stars and the image zero-point (abbreviated as “ZP” therein).

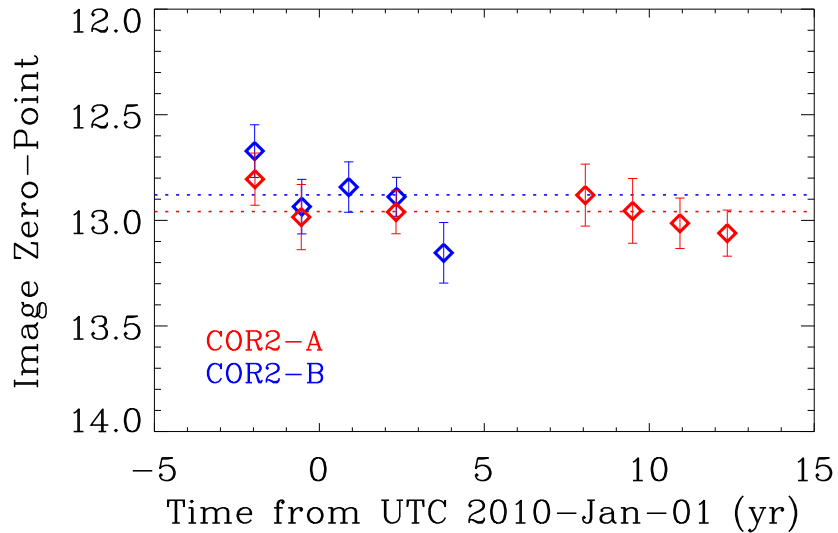


**Figure 4.** Zero-points of COR2 images in their respective bandpasses versus time. Data points of COR2-A and COR2-B are plotted in red and blue, respectively. The dotted lines are weighted mean zero-point values of the two cameras. There is tentative evidence that the zero-points have been changing over time, however, the uncertainties are too large for further interpretation.

Here,  $\phi_d$  and  $\phi_n$  are respectively the phase functions of the ejected dust and the nucleus of Phaethon (both normalised at zero phase angle),  $m_\odot$  is the apparent magnitude of the Sun in the COR2 photometric system at the mean Sun-Earth distance  $r_\oplus = 1$  au, which we obtained using the apparent magnitude of the Sun in the Pan-STARRS photometric system by Willmer (2018) and the photometric parameters in Section 3.1, and  $p$  and  $R_n$  are respectively the geometric albedo and the mean radius of Phaethon, adopted in accordance with Masiero et al. (2019). However, Equation (4) cannot be directly applicable, because our results were obtained from image stacks combined from multiple individual exposures, during which time the observing geometry of Phaethon varied nontrivially (see Table 1). Instead, we derived the correct form for conversion from the measured apparent magnitude (including the  $3\sigma$  lower limits thereof) of Phaethon in the stacks ( $\bar{m}$ ) to the time-average effective cross-section of ejected dust to be

$$\bar{\Xi}_d = \pi \left[ \frac{t_2 - t_1}{pr_\oplus^2} 10^{0.4(m_\odot - \bar{m})} - R_n^2 \int_{t_1}^{t_2} \frac{\phi_n(\alpha)}{r_H^2 \Delta^2} dt \right] \cdot \left[ \int_{t_1}^{t_2} \frac{\phi_d(\alpha)}{r_H^2 \Delta^2} dt \right]^{-1}, \quad (5)$$

where  $t_1$  and  $t_2$  are the start and end epochs of images used for stacking. We adopted the best-fit phase function by Tabeshian et al. (2019), which sampled phase angles from  $\sim 20^\circ$  to  $100^\circ$ , as the phase function of Phaethon's nucleus and approximated the phase function of dust by the empirical Halley-Marcus model, which is applicable for cometary dust with grain sizes comparable to the transmitted wavelengths (Marcus 2007; Schleicher & Bair 2011). The uncertainty in  $\bar{\Xi}_d$  was properly propagated from errors in our photometric measurements, the adopted thermophysical parameters, and the phase function of the nucleus.

Here, a few remarks are deserved on the validity of the adopted phase function of dust. Although the model is in good agreement with numerous comets even at large phase angles  $\lesssim 170^\circ$  (Marcus 2007; Hui 2013), it is also well known that scattering of dust can be affected by various physical properties of dust, including the grain size, shape, porosity, and composition, and therefore discrepancies with the model may occur. The major difference of the phase function is in the forward-scattering regime as a result of diffraction, which is primarily dependent on the dust grain size (Kolokolova et al. 2004; Marcus 2007, and citations therein). In reality, forward scattering of dust grains may be much more narrowly confined to higher phase angles (e.g., Muñoz et al. 2020), even beyond the coverage of the COR2 observations of Phaethon. However, this will require mm-sized or larger dust grains, not only order-of-magnitude greater than the transmitted wavelengths of the COR2 cameras, but also inconsistent with the inference of the anomalous brightening of Phaethon around perihelion caused by  $\sim 1 \mu\text{m}$  sized dust from the HI-1 observations (Jewitt & Li 2010; Jewitt et al. 2013; Li & Jewitt 2013; Hui & Li 2017). Furthermore, had a considerable amount of large dust grains been ejected from Phaethon, postperihelion observations would easily show a debris trail similar to the one of 323P/SOHO (Hui et al. 2022) but have not (Hsieh & Jewitt 2005), thereby suggesting the insignificance of large dust grains in the ejecta of Phaethon. Given these, we think that our choice of the empirical Halley-Marcus model is appropriate for the putative dust grains of Phaethon.

We append the computed values of  $\bar{\Xi}_d$  of Phaethon to Table 2, in the column of ‘‘Cross-section’’. As one can immediately notice, the observed brightness of Phaethon in the COR2 images was totally consistent with the contribution from a bare nucleus. In other words, there is no compelling evidence from the COR2 observations that Phaethon exhibited a brightness excess due to dust ejection around perihelion passages. Given the adopted phase function for dust, the most stringent constraints on the amount of dust ejected around perihelion are provided by the nondetection observations taken at large phase angles ( $\alpha \gtrsim 150^\circ$ ) due to forward scattering, which would enhance the intensity of the dust over ten times in comparison to other illumination geometry. On the other hand, the nucleus would only have  $\lesssim 1\%$  of the brightness at zero phase angles, making its contribution (the second term in Equation 5) completely negligible. Assuming that the ejected dust grains are spherical, with a mean radius of  $\bar{a}_d$  and a bulk density of  $\rho_d$ , we can estimate the ejected mass from the effective cross-section of the dust through

$$\bar{M}_d = \frac{4}{3} \rho_d \bar{a}_d \bar{\Xi}_d. \quad (6)$$

Substituting with  $\bar{a}_d \sim 1 \mu\text{m}$  and  $\rho_d = 2.6 \text{ g cm}^{-3}$  (Borovička et al. 2010), we obtain the  $3\sigma$  upper limit to the mass of ejected dust during a perihelion passage from the observations at large phase angles is  $\lesssim 10^3 \text{ kg}$ , which is at least an order of magnitude lower than the values reported by previous studies based on HI-1 observations. Thus, it seems highly unlikely that the observed perihelion activity of Phaethon in HI-1 was caused by the ejection of  $\mu\text{m}$ -sized dust particles.

The COR2 observations at small phase angles also provide us with a constraint on large (at least mm-sized) dust particles shed around perihelion in a manner similar to near-Sun object 323P/SOHO (Hui et al. 2022), albeit less



stringent than the constraint for smaller dust grains. Assuming that the debris has light scattering properties similar to the nucleus of Phaethon, their total effective cross-section can then be calculated from Equation (5) with the phase function of dust  $\phi_d$  now approximated by the one of the nucleus therein. What we found is that, based on the COR2 observations at small phase angles, the upper limit to the effective cross-section of the debris would be  $\sim 1.7 \pm 0.1$  times larger than the values for  $\sim 1 \mu\text{m}$  sized dust listed in Table 1, i.e.,  $\overline{\Sigma}_d \lesssim 10^8 \text{ m}^2$ . On the contrary, observations of 323P were able to reveal its debris trail consisting of mm-sized and larger dust grains with an effective total cross-section of  $\gtrsim 10^5 \text{ m}^2$  within two months after the perihelion passage in 2021 (Hui et al. 2022). We are unaware of any published literature that reported attempts to search for debris of Phaethon in a similar time window after perihelion. The closest was the attempt by Hsieh & Jewitt (2005), who observed Phaethon about three months after the perihelion passage in 2003 and accordingly placed an upper limit to the effective cross-section of dust to be  $\lesssim 10^5 \text{ m}^2$ . Yet given the fact that large debris would be relatively insusceptible to the solar radiation pressure, we posit that the COR2 observations at small phase angles do not set a constraint on the debris trail of Phaethon tighter than the one based on ground-based observation by Hsieh & Jewitt (2005). The fact that the debris trail of Phaethon is as yet undetected likely implies that large dust grains play a negligible role in the perihelion activity of the object, and/or that the ejection of these grains is a rare event with the occurrence rate of once in every  $\gtrsim 40$  years, given the discovery time of Phaethon. Nevertheless, we encourage future observations of Phaethon to be conducted using facilities far more sensitive than the COR2 cameras soon after perihelion so as to better search for the debris trail that might resemble the one of 323P/SOHO when opportunities arise (see Section 4).

#### 4. DISCUSSION

The COR2 observations of Phaethon clearly render the hypothesis that the observed perihelion activity at the asteroid is due to the ejection of dust problematic. One may argue that the COR2 observations have just been so unlucky that the anomalous brightening events around perihelion all occurred outside the FOVs of the cameras. By checking the ephemeris, we find that this is not the case whatsoever. While indeed there were observations that only covered the preperihelion leg of Phaethon’s orbit (COR2-A in 2009, 2012, 2018, 2019, and 2022, and the perihelion was barely observed right before the egress of Phaethon’s transit in 2020, and COR2-B in 2010), the rest covered the periods in which the anomalous brightening would be expected to take place. For instance, the amount of micron-sized dust ejected during the anomalous brightening at the perihelion return in 2009 reported by Jewitt & Li (2010) would have produced a strong forward-scattering enhancement easily detectable in the COR2-B images, as Phaethon was also well inside the FOV of the coronagraphic camera. Since the perihelion activity of Phaethon was alike from apparition to apparition (Jewitt & Li 2010; Li & Jewitt 2013; Hui & Li 2017), we expect that the other observations in which the postperihelion leg of the orbit was monitored would also encounter the same conundrum. On the other hand, the unobserved forward scattering in the COR2 data would be consistent with scattering properties of mm-sized or larger dust grains. However, postperihelion observations of Phaethon should then easily detect the debris trail as in the case of 323P/SOHO (Hui et al. 2022) but did not. Furthermore, this type of dust grains are completely incompatible with the  $\mu\text{m}$ -sized ones inferred from the HI-1 observations. Therefore, we can firmly conclude that the observed perihelion activity of Phaethon is not caused by dust, but by some fluorescence emissions transmittable to the HI-1 but not COR2 cameras onboard the STEREO spacecraft.

The bandpasses of the HI-1 and COR2 cameras largely overlap with each other. However, there are still two noticeable differences: 1) the main bandpasses of the HI-1 cameras cover systematically shorter wavelengths, and 2) the HI-1 cameras have a nontrivial blue leak in their bandpasses around  $\sim 400 \text{ nm}$  (Bewsher et al. 2010). Therefore, we speculate that strong fluorescence emissions produced during the near-Sun activity of Phaethon lies within either of the regions, or both. Associated with previous observations of comets such as C/1965 S1 (Ikeya-Seki) and C/2006 P1 (McNaught) at similar heliocentric distances (Preston 1967; Fulle et al. 2007), and given the study by Manfroid et al. (2021) finding that free iron atoms prevail in comae of comets even at larger heliocentric distances, we boldly conjecture the Fe I emission lines around  $\lambda \approx 400 \text{ nm}$  being a promising possibility. The conjecture does not conflict with the model prediction by Lisse & Steckloff (2022) that Phaethon can develop a coma comprised of iron gas around perihelion. Obviously, future observations of the asteroid are needed to verify the thermophysical model by Lisse & Steckloff (2022) and our conjecture.

Besides, we are aware that Mercury was observed to possess an anti-sunward tail in images taken by the HI-1 cameras on multiple occasions (Schmidt 2013). Given the effective transmission of the HI-1 cameras, the tail appeared to be too bright to be accounted for by sodium D emissions, unless degradation has occurred to the HI-1 cameras

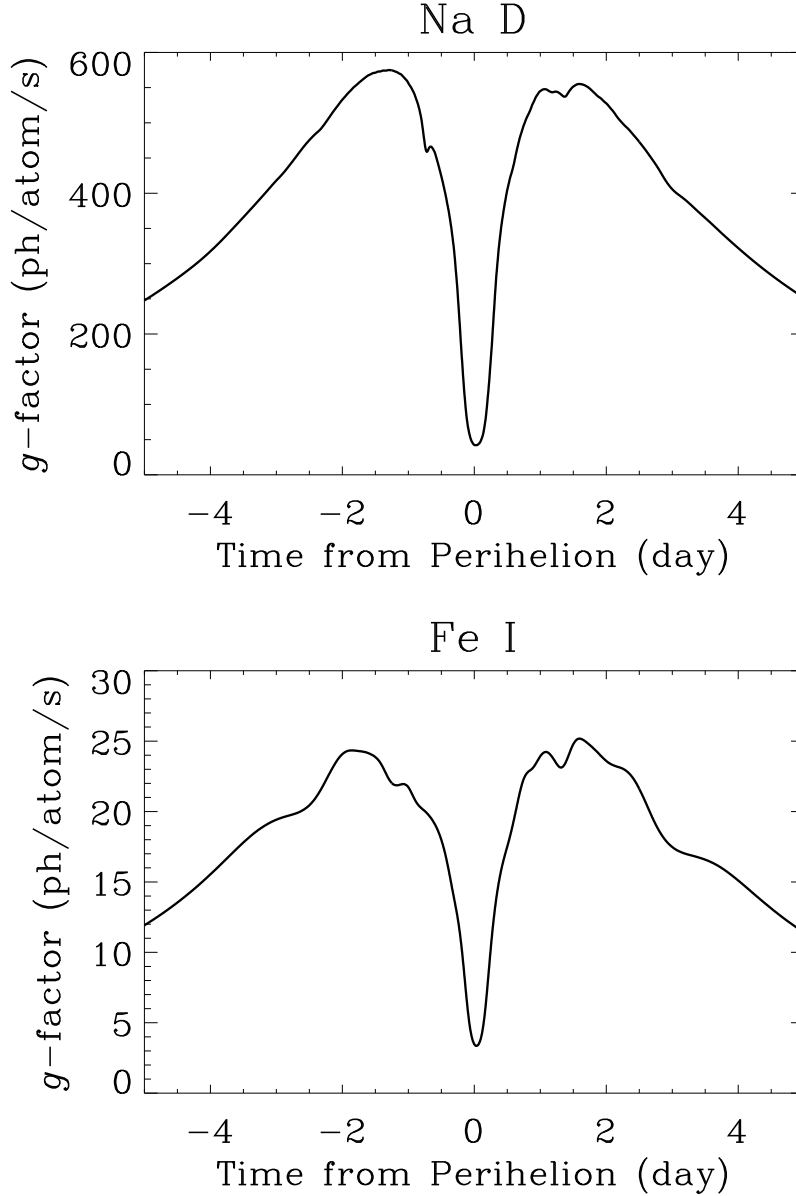


**Figure 5.** Fluorescence efficiencies ( $g$ -factors, in the unit of photons per atom per second) of Fe I (upper panel) and Na D (lower panel) emissions in the current orbit of Phaethon around perihelion. The dips at perihelion are due to the overlaps with the solar Fraunhofer absorption lines.

that caused a change in their bandpasses, making sodium D emission lines transmittable (Schmidt 2013). Recently, Price et al. (2022) reported the identification of a prominent neutral sodium tail at comet C/2011 L4 (PANSTARRS) in HI-1 observations, whereby they also suspected a considerable shift in the bandpass of the camera. Unfortunately, we are unaware of any published literature on measuring the ageing effects of the HI-1 filters. Instead, the focus was primarily on the detector sensitivity, which was reported to have little sign of degradation (Bewsher et al. 2012). Although the STEREO team did notice a shift in the bandpasses, relevant details are yet to be characterised (K. Battams, private communication). More recently, Zhang et al. (in preparation) analysed observations of Phaethon around its latest perihelion return in 2022 May from the SOHO spacecraft (Domingo et al. 1995), finding that it was only visible through the orange filter. The markedly higher intensities of near-Sun comets in the orange filters are believed to be caused by the sodium D emissions (Knight et al. 2010). By the same token, Zhang et al. suggested

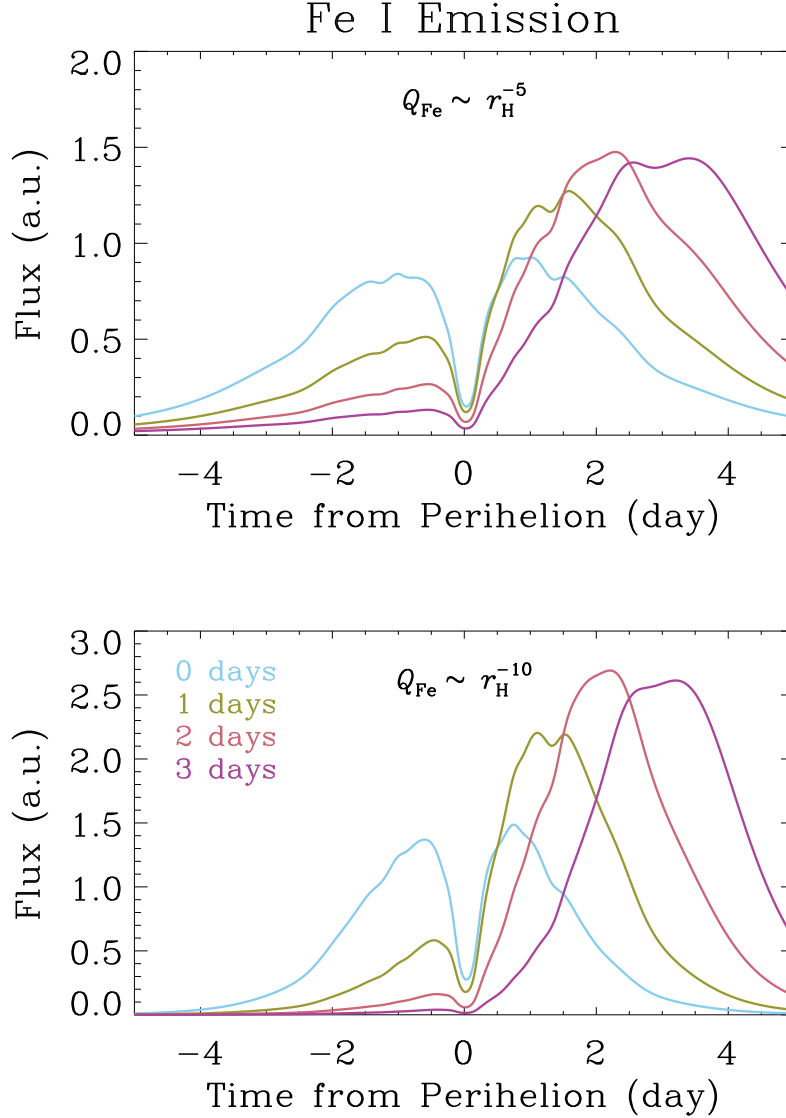


**Figure 6.** Modelled flux (in arbitrary units) of Phaethon due to Fe I emissions transmittable in the HI-1 cameras (wavelengths  $\lambda \approx 400$  nm). In the top panel, the production rate of iron is assumed to be  $\sim r_{\text{H}}^{-5}$ , whereas  $\sim r_{\text{H}}^{-10}$  is assumed in the bottom panel. Different colours of the curves correspond to the peak of the iron production rate delayed by different amounts of time (labelled in the legend) from perihelion.

to us that the sodium emissions likely dominated the observed signal of Phaethon in the SOHO images. In addition, they analysed earlier SOHO and HI-1 observations, arriving at the same conclusion that the sodium emissions most likely played a crucial role in causing the observed anomalous brightening of the object around perihelion. Taking into account the fact that sodium emissions have been observed in many comets at heliocentric distances  $\lesssim 0.7$  au, the length and brightness of sodium tails of comets are found to climax at heliocentric distances in a range of  $\sim 0.1$ - $0.2$  au (Huebner 1970), and the results from the thermophysical modelling and laboratory experiments by Masiero et al. (2021) that sodium emissions around perihelion passages of Phaethon are capable of producing the observed activity, here we also include sodium emissions to form a comparison to the results with iron emissions.

In the following, we apply a simplistic model to briefly assess if Fe I and/or sodium D emissions can qualitatively reproduce the observed flareup in the brightness of Phaethon around its perihelion passages (Jewitt & Li 2010; Li & Jewitt 2013; Hui & Li 2017). A more sophisticated model for application of the sodium emissions will be separately presented by Zhang et al. (in preparation). First, we need to compute the fluorescence efficiency, or called the  $g$ -factor,

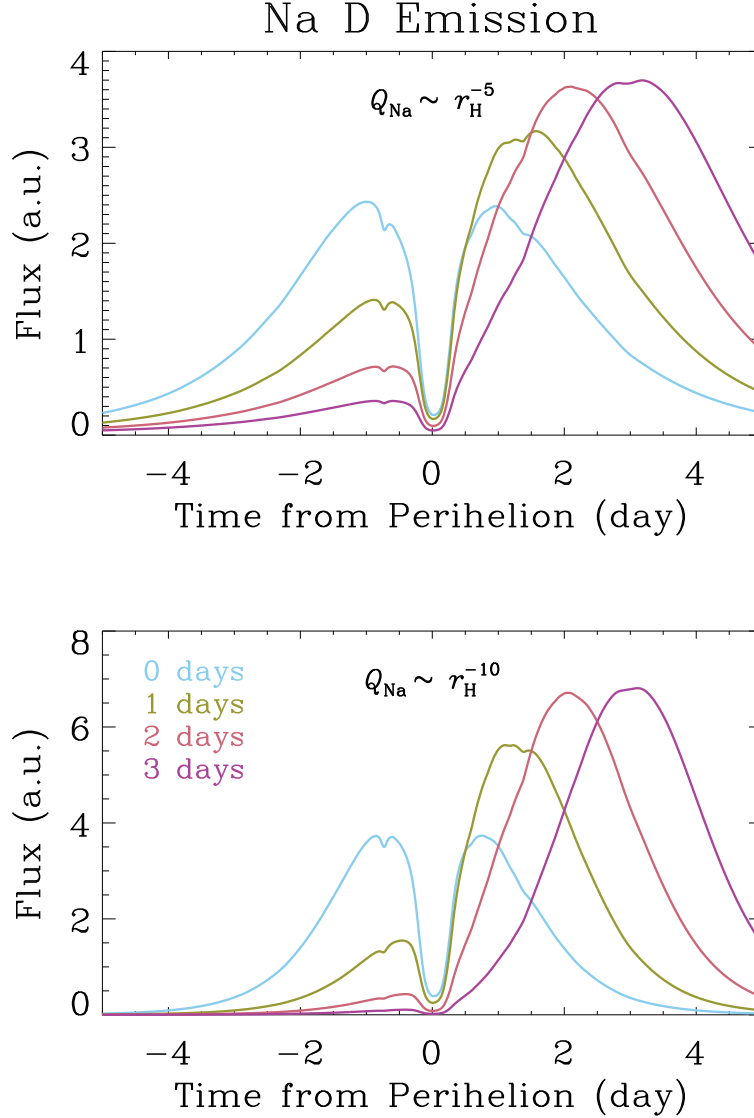


**Figure 7.** Same as Figure 6, but for Na D-line emissions.

which essentially describes the rate at which an atomic species absorbs photons, from (c.f. [Smyth 1979](#))

$$g(r_{\text{H}}, \dot{r}_{\text{H}}) = \gamma(\dot{r}_{\text{H}}) \frac{q_e^2 f \lambda^3 F_{\lambda}}{8 \varepsilon_0 \hbar m_e c^3} \left( \frac{r_{\oplus}}{r_{\text{H}}} \right)^2. \quad (7)$$

Here, the fluorescence efficiency is a function of both the heliocentric distance and the rate thereof,  $\gamma$  is the fraction of the Doppler-shifted solar incident flux relative to the solar continuum, whose spectral radiance per unit wavelength is denoted as  $F_{\lambda}$ ,  $f$  is the absorption oscillator strength,  $q_e = 1.6 \times 10^{-19}$  C is the elementary charge,  $\hbar = 1.1 \times 10^{-34}$  J s $^{-1}$  is the reduced Planck's constant,  $\varepsilon_0 = 8.9 \times 10^{-12}$  F m $^{-1}$  is the vacuum permittivity,  $m_e = 9.1 \times 10^{-31}$  kg is the electron mass, and  $c = 3.0 \times 10^8$  m s $^{-1}$  is the speed of light. Physical parameters for sodium D and Fe I emission lines were taken from [Steck \(2010\)](#) and [Morton \(2003\)](#), respectively, and the high-resolution solar spectrum atlas by [Kurucz et al. \(1984\)](#) was used in the calculation. The fluorescence efficiencies in the current orbit of Phaethon within five days from perihelion are plotted in Figure 5.

Next, we assumed various heliocentric dependencies for the atomic production rates  $Q$  of iron and sodium atoms. In our simplistic model, the total flux due to the fluorescence emission is proportional to  $gQ\tau$ , where  $\tau$  is the pho-

toionisation lifetime scaled as the square of the heliocentric distance. We adopted the photoionisation lifetimes of iron and sodium based on Huebner & Mukherjee (2015). Given the HI-1 observations of the peak flux of Phaethon during the near-Sun activity, we can then estimate the corresponding production rates of iron and sodium to be  $Q_{\text{Fe}} \sim 10^{25} \text{ s}^{-1}$  and  $Q_{\text{Na}} \sim 10^{24} \text{ s}^{-1}$ , respectively. In comparison, Fulle et al. (2007) analysed also the HI-1 images and reported a production rate of  $Q_{\text{Fe}} \sim 10^{30} \text{ s}^{-1}$  for comet C/2006 P1 (McNaught) at heliocentric distance  $r_{\text{H}} = 0.25 \text{ au}$ . Bromley et al. (2021) and Manfroid et al. (2021) measured the production rates of iron to be  $Q_{\text{Fe}} \sim 10^{21}\text{--}10^{24} \text{ s}^{-1}$  for a list of comets at heliocentric distances of  $\sim 0.7\text{--}3 \text{ au}$ . As for sodium, for instance, comet C/1995 O1 (Hale-Bopp) was measured to produce sodium atoms at a rate of  $\sim 10^{25}\text{--}10^{26} \text{ s}^{-1}$  at  $\sim 1 \text{ au}$  from the Sun (Cremonese et al. 1997; Rauer et al. 1998; Wilson et al. 1998), and C/2012 S1 (ISON) had  $Q_{\text{Na}} \sim 10^{23}\text{--}10^{24} \text{ s}^{-1}$  (Schmidt et al. 2015). Here, with the comparisons we do not mean to suggest that sodium and iron are produced in a common manner at Phaethon and the aforementioned comets at larger heliocentric distances; the process occurring at Phaethon near perihelion is possibly confined to the near-Sun environment only, where the surface temperature can be heated up to  $>1000 \text{ K}$ .

The obtained general shapes of the emissions due to Fe I and Na D lines are closely similar, both of which brighten around perihelion but drop considerably at perihelion, because of the overlaps with the solar Fraunhofer absorption lines. In reality, the behaviour of the perihelion activity of Phaethon is observed to be repetitive in different perihelion apparitions, which peaks approximately a day after perihelion passage (Jewitt & Li 2010; Li & Jewitt 2013; Hui & Li 2017). This is likely a consequence of the thermophysical heterogeneity due to the spin-axis orientation of Phaethon (MacLennan et al. 2022), whereby the northern hemisphere is possibly more thermally processed and the southern one is suddenly exposed to sunlight soon after perihelion (Ohtsuka et al. 2009; Ansdell et al. 2014; Yu et al. 2019). Therefore, we arbitrarily shifted the peak of the production rate by 1-3 days past perihelion in the same fashion as in the asymmetric outgassing model for cometary nongravitational forces (Yeomans & Chodas 1989), and recomputed the emission fluxes. We show the results for Fe I and Na D emissions respectively in Figures 6 and 7, in which we can see the best similarity to the HI-1 photometry of Phaethon is given by the asymmetric models with a delay of one or two days in the peak production rate.

Admittedly, at the current stage, by no means can we affirm that the observed perihelion activity of Phaethon is due to iron and/or sodium emissions, but we posit that the hypothesis is a promising one, in that it has no conspicuous conflict with the HI-1 and COR2 observations, whereas the dust hypothesis encounters severe difficulties. In order to identify which specific gas species are the cause of the perihelion activity of Phaethon, the only feasible way is to observe the asteroid close to the Sun as much as possible, ideally at heliocentric distances  $\lesssim 1 \text{ au}$ , given the fact that sodium emissions have been observed at many comets at  $r_{\text{H}} \lesssim 1 \text{ au}$ , mostly  $\lesssim 0.7 \text{ au}$  (Huebner 1970). We expect that in-situ measurements from the upcoming DESTINY+ mission (Arai et al. 2018), which is presently planned to have a flyby with Phaethon at a heliocentric distance of  $0.87 \text{ au}$  in 2026 August (Krüger et al. 2019), may be able to test our gas hypothesis.

To facilitate future ground observations of Phaethon, we exploited JPL Horizons to search for potential future ideal observing windows of Phaethon at heliocentric distances  $r_{\text{H}} \leq 1 \text{ au}$  while at solar elongations  $\geq 50^\circ$  by the end of this century. The opportunities in the next decade are tabulated in Table 3. These will still be applicable for telescopes that are capable of reaching lower solar elongations, just that the observing windows will be wider. Given the current orbit, unfortunately Phaethon can never be observed at  $r_{\text{H}} \leq 0.7 \text{ au}$  and solar elongations  $\gtrsim 50^\circ$  simultaneously from the ground in the investigated period of time. However, we managed to identify a number of observing windows of Phaethon at even smaller heliocentric distances during total solar eclipses by the end of the century, during which time searching for gas emissions of the asteroid will be feasible for ground observations (see also Table 3). The best of all opportunities will be during the total solar eclipse on 2089 October 4, soon after the perihelion passage of Phaethon, when the asteroid will be at a heliocentric distance of  $\sim 0.16 \text{ au}$  and  $\sim 8^\circ$  from the Sun. Far more observations of Phaethon at small heliocentric distances will be certainly needed for us to fully understand the near-Sun activity of the object.

## 5. SUMMARY

We studied near-Sun asteroid (3200) Phaethon using coronagraphic observations taken by the COR2 cameras onboard the STEREO spacecraft around different perihelion returns. The key findings are:



**Table 3.** Future Ideal Observing Windows of Phaethon

Observable Date (UT)	Heliocentric Distance $r_H$ (au)	Geocentric Distance $\Delta$ (au)	Solar Elongation $\varepsilon$ ( $^\circ$ )	Phase Angle $\alpha$ ( $^\circ$ )
2023 Nov 17 – 2023 Nov 28	0.791 $\rightarrow$ 0.992	0.788 $\rightarrow$ 0.898	51.4 $\rightarrow$ 63.3	77.6 $\rightarrow$ 62.7
2025 Feb 17 – 2025 Feb 24	0.996 $\rightarrow$ 0.873	1.083 $\rightarrow$ 1.066	57.3 $\rightarrow$ 50.1	56.5 $\rightarrow$ 60.4
Total Solar Eclipse on 2026 Aug 12	0.648	1.542	17.2	27.6
2026 Oct 1 – 2016 Oct 10 <sup>†</sup>	0.823 $\rightarrow$ 0.986	0.387 $\rightarrow$ 0.368	52.2 $\rightarrow$ 77.3	106.0 $\rightarrow$ 81.3
2027 Dec 31 – 2028 Jan 11	1.000 $\rightarrow$ 0.801	0.290 $\rightarrow$ 0.379	84.8 $\rightarrow$ 50.9	78.4 $\rightarrow$ 107.5
2029 Aug 12 – 2029 Aug 23	0.798 $\rightarrow$ 0.998	0.809 $\rightarrow$ 0.824	50.4 $\rightarrow$ 64.9	78.1 $\rightarrow$ 66.6
2030 Nov 13 – 2030 Nov 24	0.990 $\rightarrow$ 0.789	0.546 $\rightarrow$ 0.465	74.0 $\rightarrow$ 51.7	74.0 $\rightarrow$ 100.8
Total Solar Eclipse on 2030 Nov 25	0.763	0.466	48.5	104.2
Total Solar Eclipse on 2078 May 11	0.813	1.672	20.9	26.3
Total Solar Eclipse on 2082 Aug 24	0.694	0.632	42.6	99.3
Total Solar Eclipse on 2088 Apr 21	0.250	0.961	14.4	92.9
Total Solar Eclipse on 2089 Oct 4	0.158	1.049	8.4	67.9
Total Solar Eclipse on 2094 Jan 16	0.215	0.832	9.7	129.8
Total Solar Eclipse on 2095 Jun 2	0.764	1.755	8.2	10.8
Total Solar Eclipse on 2099 Sep 14	0.863	1.385	38.3	46.3

<sup>†</sup> The perigee will occur approximately on 2026 Oct 8 at a distance of  $\Delta \approx 0.365$  au.

NOTE—The observing geometry of Phaethon during a total solar eclipse is referred to the corresponding time of greatest eclipse given at <https://eclipse.gsfc.nasa.gov/SEcat5/SE2001-2100.html>.

1. Phaethon could only be seen around perihelion at small ( $\lesssim 30^\circ$ ) but not large phase angles ( $\gtrsim 150^\circ$ ) in the combined stacks of images, which means that the previously reported near-Sun activity of Phaethon based on HI-1 observations lacks a strong forward scattering effect, contradictory to what dust having sizes comparable to transmitted wavelengths would undergo.
2. Using the nondetection observations, we obtained that the amount of micron-sized dust grains ejected during a perihelion passage is at least an order of magnitude lower than previous estimates based on HI-1 observations.
3. In fact, the observed brightness of Phaethon in the COR2 observations was measured to be consistent with the contribution from a bare nucleus, suggesting that the signal from the perihelion activity recorded in HI-1 is not transmittable to the COR2 cameras at all.
4. We thereby conclude that the observed near-Sun activity of Phaethon is highly unlikely due to the ejection of dust. Rather, we speculate that the activity is possibly accounted for by Fe I and/or Na D emission lines, the latter of which may have become transmittable to the HI-1 cameras because of the ageing effect.
5. We modelled the fluxes of Phaethon due to Fe I and Na D emissions, finding that the asymmetric models in which the peak of the atomic production rate is delayed by  $\sim 1$  day from perihelion can best reproduce a lightcurve visually similar to the observations in the HI-1 cameras.
6. More observations of Phaethon at small heliocentric distances will be needed to search for the gas emissions and to fully understand the near-Sun activity of the asteroid. We identified a list of observing windows ideal for future ground observations, the best of which will be during total solar eclipses.

## ACKNOWLEDGMENTS

We thank Bin Yang, Karl Battams, and William Thompson for their help and Qicheng Zhang for discussions and the anonymous reviewer for providing insightful comments on our manuscript. We thank also Frederic A. Rasio spending time reviewing the manuscript and commenting that our work is of rather limited interest to the research community as a whole. This work was supported by the Science and Technology Development Fund, Macau SAR, through grant No. SKL-LPS (MUST)-2021-2023.

*Facilities:* STEREO

*Software:* `astrometry.net` (Lang et al. 2010), IDL, MPFIT (Markwardt 2009), SSW (Freeland & Handy 1998)

## REFERENCES

- Ansdell, M., Meech, K. J., Hainaut, O., et al. 2014, *ApJ*, 793, 50. doi:10.1088/0004-637X/793/1/50
- Arai, T., Kobayashi, M., Ishibashi, K., et al. 2018, 49th Annual Lunar and Planetary Science Conference
- Arendt, R. G. 2014, *AJ*, 148, 135. doi:10.1088/0004-6256/148/6/135
- Battams, K., Knight, M. M., Kelley, M. S. P., et al. 2020, *ApJS*, 246, 64. doi:10.3847/1538-4365/ab6c68
- Battams, K., Gutarra-Leon, A. J., Gallagher, B. M., et al. 2022, *ApJ*, 936, 81. doi:10.3847/1538-4357/ac83b5
- Bewsher, D., Brown, D. S., Eyles, C. J., et al. 2010, *SoPh*, 264, 433. doi:10.1007/s11207-010-9582-8
- Bewsher, D., Brown, D. S., & Eyles, C. J. 2012, *SoPh*, 276, 491. doi:10.1007/s11207-011-9874-7
- Borovička, J., Kolen, P., Spurný, P., et al. 2010, *Icy Bodies of the Solar System*, 263, 218. doi:10.1017/S174392131000178X
- Bromley, S. J., Neff, B., Loch, S. D., et al. 2021, *PSJ*, 2, 228. doi:10.3847/PSJ/ac2dff
- Chamberlin, A. B., McFadden, L.-A., Schulz, R., et al. 1996, *Icarus*, 119, 173. doi:10.1006/icar.1996.0009
- Cochran, A. L. & Barker, E. S. 1984, *Icarus*, 59, 296. doi:10.1016/0019-1035(84)90029-0
- Cremonese, G., Boehnhardt, H., Crovisier, J., et al. 1997, *ApJL*, 490, L199. doi:10.1086/311040
- Domingo, V., Fleck, B., & Poland, A. I. 1995, *SoPh*, 162, 1. doi:10.1007/BF00733425
- Eyles, C. J., Harrison, R. A., Davis, C. J., et al. 2009, *SoPh*, 254, 387. doi:10.1007/s11207-008-9299-0
- Freeland, S. L. & Handy, B. N. 1998, *SoPh*, 182, 497. doi:10.1023/A:1005038224881
- Fulle, M. 2004, *Comets II*, 565
- Fulle, M., Leblanc, F., Harrison, R. A., et al. 2007, *ApJL*, 661, L93. doi:10.1086/518719
- Green, S. & Kowal, C. 1983, *IAUC*, 3878
- Howard, R. A., Moses, J. D., Vourlidas, A., et al. 2008, *SSRv*, 136, 67. doi:10.1007/s11214-008-9341-4
- Hsieh, H. H. & Jewitt, D. 2005, *ApJ*, 624, 1093. doi:10.1086/429250
- Huebner, W. F. 1970, *A&A*, 5, 286
- Huebner, W. F. & Mukherjee, J. 2015, *Planet. Space Sci.*, 106, 11. doi:10.1016/j.pss.2014.11.022
- Hui, M.-T. 2013, *MNRAS*, 436, 1564. doi:10.1093/mnras/stt1683
- Hui, M.-T. & Li, J. 2017, *AJ*, 153, 23. doi:10.3847/1538-3881/153/1/23
- Hui, M.-T., Tholen, D. J., Kracht, R., et al. 2022, *AJ*, 164, 1. doi:10.3847/1538-3881/ac6dcb
- Jenniskens, P. 2006, *Meteor Showers and their Parent Comets*, by Peter Jenniskens, pp. . ISBN 0521853494. Cambridge, UK: Cambridge University Press, 2006.
- Jewitt, D. & Li, J. 2010, *AJ*, 140, 1519. doi:10.1088/0004-6256/140/5/1519
- Jewitt, D. 2012, *AJ*, 143, 66. doi:10.1088/0004-6256/143/3/66
- Jewitt, D., Li, J., & Agarwal, J. 2013, *ApJL*, 771, L36. doi:10.1088/2041-8205/771/2/L36
- Jewitt, D., Hsieh, H., & Agarwal, J. 2015, *Asteroids IV*, 221. doi:10.2458/azu\_uapress\_9780816532131-ch012
- Jewitt, D., Mutchler, M., Agarwal, J., et al. 2018, *AJ*, 156, 238. doi:10.3847/1538-3881/aae51f
- Jewitt, D., Asmus, D., Yang, B., et al. 2019, *AJ*, 157, 193. doi:10.3847/1538-3881/ab13a9
- Jewitt, D. & Hsieh, H. H. 2022, arXiv:2203.01397
- Kaiser, M. L., Kucera, T. A., Davila, J. M., et al. 2008, *SSRv*, 136, 5. doi:10.1007/s11214-007-9277-0
- Knight, M. M., A’Hearn, M. F., Biesecker, D. A., et al. 2010, *AJ*, 139, 926. doi:10.1088/0004-6256/139/3/926
- Kolokolova, L., Hanner, M. S., Levasseur-Regourd, A.-C., et al. 2004, *Comets II*, 577

- Krüger, H., Strub, P., Srama, R., et al. 2019, *Planet. Space Sci.*, 172, 22. doi:10.1016/j.pss.2019.04.005
- Kurucz, R. L., Furenlid, I., Brault, J., et al. 1984, *National Solar Observatory Atlas, Sunspot*, New Mexico: National Solar Observatory, 1984
- Lang, D., Hogg, D. W., Mierle, K., et al. 2010, *AJ*, 139, 1782. doi:10.1088/0004-6256/139/5/1782
- Li, J. & Jewitt, D. 2013, *AJ*, 145, 154. doi:10.1088/0004-6256/145/6/154
- Lisse, C. M. & Steckloff, J. K. 2022, *Icarus*, 381, 114995. doi:10.1016/j.icarus.2022.114995
- Lodders, K. 2003, *ApJ*, 591, 1220. doi:10.1086/375492
- Manfroid, J., Hutsemékers, D., & Jehin, E. 2021, *Nature*, 593, 372. doi:10.1038/s41586-021-03435-0
- Marcus, J. N. 2007, *International Comet Quarterly*, 29, 39
- Masiero, J. R., Wright, E. L., & Mainzer, A. K. 2019, *AJ*, 158, 97. doi:10.3847/1538-3881/ab31a6
- Masiero, J. R., Davidsson, B. J. R., Liu, Y., et al. 2021, *PSJ*, 2, 165. doi:10.3847/PSJ/ac0d02
- Markwardt, C. B. 2009, *Astronomical Data Analysis Software and Systems XVIII*, 411, 251
- MacLennan, E., Marshall, S., & Granvik, M. 2022, arXiv:2203.08865
- Morton, D. C. 2003, *ApJS*, 149, 205. doi:10.1086/377639
- Muñoz, O., Moreno, F., Gómez-Martín, J. C., et al. 2020, *ApJS*, 247, 19. doi:10.3847/1538-4365/ab6851
- Ohtsuka, K., Sekiguchi, T., Kinoshita, D., et al. 2006, *A&A*, 450, L25. doi:10.1051/0004-6361:200600022
- Ohtsuka, K., Arakida, H., Ito, T., et al. 2008, *Meteoritics and Planetary Science Supplement*, 43, 5055
- Ohtsuka, K., Nakato, A., Nakamura, T., et al. 2009, *PASJ*, 61, 1375. doi:10.1093/pasj/61.6.1375
- Preston, G. W. 1967, *ApJ*, 147, 718. doi:10.1086/149049
- Price, O., Jones, G. H., Battams, K., Owens, M., et al. 2022, *Icarus*, 389, 115218. doi:10.1016/j.icarus.2022.115218
- Rauer, H., Arpigny, C., Manfroid, J., et al. 1998, *A&A*, 334, L61
- Schleicher, D. G. & Bair, A. N. 2011, *AJ*, 141, 177. doi:10.1088/0004-6256/141/6/177
- Schmidt, C. A. 2013, Ph.D. Thesis
- Schmidt, C. A., Johnson, R. E., Baumgardner, J., et al. 2015, *Icarus*, 247, 313. doi:10.1016/j.icarus.2014.10.022
- Smyth, W. H. 1979, *ApJ*, 234, 1148. doi:10.1086/157598
- Steck, D. A. 2010, *Sodium D Line Data*, <http://steck.us/alkalidata>
- Tabeshian, M., Wiegert, P., Ye, Q., et al. 2019, *AJ*, 158, 30. doi:10.3847/1538-3881/ab245d
- Tonry, J. L., Denneau, L., Flewelling, H., et al. 2018, *ApJ*, 867, 105. doi:10.3847/1538-4357/aae386
- Whipple, F. L. 1983, *IAUC*, 3881
- Wiegert, P. A., Houde, M., & Peng, R. 2008, *Icarus*, 194, 843. doi:10.1016/j.icarus.2007.12.013
- Williams, I. P. & Wu, Z. 1993, *MNRAS*, 262, 231. doi:10.1093/mnras/262.1.231
- Willmer, C. N. A. 2018, *ApJS*, 236, 47. doi:10.3847/1538-4365/aabfdd
- Wilson, J. K., Baumgardner, J., & Mendillo, M. 1998, *Geophys. Res. Lett.*, 25, 225. doi:10.1029/97GL03704
- Ye, Q., Wiegert, P. A., & Hui, M.-T. 2018, *ApJL*, 864, L9. doi:10.3847/2041-8213/aada46
- Ye, Q., Knight, M. M., Kelley, M. S. P., et al. 2021, *PSJ*, 2, 23. doi:10.3847/PSJ/abcc71
- Yeomans, D. K. & Chodas, P. W. 1989, *AJ*, 98, 1083. doi:10.1086/115198
- Yu, L. L., Ip, W. H., & Spohn, T. 2019, *MNRAS*, 482, 4243. doi:10.1093/mnras/sty3023